Ab initio prediction of specific phospholipid complexes and membrane association of HIV-1 MPER antibodies by multi-scale simulations

Colleen Maillie[1], Jay Golden[1], Ian A. Wilson[1], Andrew B. Ward[1], Marco Mravic[1,*]

[1]Department of Integrative Structural and Computational Biology, The Scripps Research Institute, La Jolla, CA, 92037, USA

[*]Corresponding author:
Marco Mravic, mmravic@scripps.edu

Summary

A potent class of HIV-1 broadly neutralizing antibodies (bnAbs) targets the envelope glycoprotein's membrane proximal exposed region (MPER) through a proposed mechanism where hypervariable loops embed into lipid bilayers and engage headgroup moieties alongside the epitope. We address the feasibility and determinant molecular features of this mechanism using integrative modeling. All-atom simulations of 4E10, PGZL1, 10E8 and LN01 docked onto HIV-like membranes consistently form phospholipid complexes at key complementarity-determining region loop sites, solidifying that stable and specific lipid interactions anchor bnAbs to membrane surfaces. Ancillary protein-lipid contacts reveal surprising contributions from antibody framework regions. Coarse-grained simulations effectively capture antibodies embedding into membranes. Simulations estimating protein-membrane interaction strength for PGZL1 variants along an inferred maturation pathway show bilayer affinity is evolved and correlates with neutralization potency. The modeling platform developed here uncovers insights into lipid participation in antibodies' recognition of membrane proteins and highlights antibody features to prioritize in vaccine design.

Keywords: Molecular Dynamics, HIV MPER, Broadly Neutralizing Antibodies, Lipid Membranes

Introduction

Antibodies can target epitopes on integral membrane proteins very near to the lipid bilayer surface, even those partially embedded within the headgroup region. In the process of engaging the antigen, antibodies complementarity-determining regions (CDR) may need to navigate interactions with or concealment by lipid molecules. Then, evolving tolerance or even affinity to lipid bilayers could be beneficial in recognition of membrane-proximal epitopes, for example gaining avidity and specificity via cooperative interactions simultaneously with the epitope and membrane. Conversely, propensity to bind lipids or cell membranes poses a significant auto-immunity risk. B-cells producing antibodies targeting host membranes are downregulated in healthy organisms[1–4]. Nonetheless, in cases of chronic inflammation and infection as in HIV, rare antibodies with lipid affinity can emerge[5–8]. The maturation pathways of these rare events remain unclear, but a careful balance of polyreactivity must be struck to avoid or overcome autoreactivity[9]. A better understanding of how antibodies develop membrane affinity and target membrane-proximal epitopes would be impactful for antibody therapeutics, auto-immunity, and vaccine development[10–12].

We sought to address this phenomenon for broadly neutralizing antibodies (bnAbs) 4E10, PGZL1, 10E8, and LN01 of unique lineages which all target the semi-concealed membrane-proximal epitope region (MPER)[13–16] of the HIV-1 envelope glycoprotein (Env). Interestingly, most of these bnAbs show affinity for lipid components and freely associate with lipid bilayers[5–8] or cultured cells, even in the absence of antigen[17–23]. This membrane interaction behavior is attributed to shared CDR loop features, including a long hydrophobic CDR-H3[7,18,21,22,24–26], and appears to correlate with neutralization potency. Engineered mutations to the 10E8 paratope at light-chain solvent-exposed residues that add positive charge or hydrophobic sidechains proved to increase antibody association to anionic phospholipid vesicles *in vitro* and also boosted neutralization potency[27]. Conversely, mutations reducing CDR-H3 hydrophobicity (e.g. 4E10 H100-H102 Trp-Trp motif to Ala-Ala or Asp-Asp) only marginally affect antigen affinity, but drastically reduce neutralization activity and weakened association to lipid bilayers in parallel[7,21,28,29].

Structural characterization of full-length Env trimer or fragments of gp41 suggest the surrounding lipid bilayer plays a role in antibody access and epitope recognition[13,30]. Cryo-electron microscopy (cryo-EM) of

bnAb-bound pre-fusion Env in different membrane environments indicate that bnAb CDR loops form intimate contacts with surrounding lipids while engaging MPER. Additionally, crystal structures of MPER-targeting bnAbs as antigen binding fragments (Fab) soaked with short-chain phospholipids revealed a spectrum of ordered headgroup moieties complexed within the CDR loops in the presence and absence of antigen, suggesting the antibodies encode specific lipid interactions[5,8,20,31,31]. Thus, the molecular features mediating membrane affinity for these bnAbs appear critical to their maturation and mechanism of immune protection against HIV *in vivo*.

These data support a 2-step bnAb neutralization mechanism proposed previously, wherein a population of bnAbs *in vivo* may first associate with membranes via embedding their CDRs, then laterally diffuse across the bilayer surface to subsequently engage Env at MPER[6,19,22,24,25,30–33]. Here, we developed multi-scale molecular dynamics (MD) simulation approaches suited to investigate this mechanism alongside the unique maturation landscape these rare antibodies must navigate to avoid auto-immune consequences. For these MPER bnAbs, we focused on the ability to model and characterize *in silico* the molecular features that mediate their lipid affinity *in vivo* at the necessary atomic detail not afforded by structural approaches used to date. We expect these and similar approaches for predicting membrane bound conformations and lipid affinity of natural and putative antibody sequences will be powerful for understanding neutralization efficacy, epitope engagement mechanisms, and the checkpoints regulating self-sensing antibodies.

Modelling bnAbs as Fabs docked onto HIV-like lipid bilayers, we find that unbiased all-atom MD simulations accurately and reproducibly predict *ab inito* binding of phospholipids at specific CDR binding sites previously identified in co-crystal structures[19,20,24,31]. Further, we demonstrate that macroscopic surface properties represented in unbiased insertion coarse grain (CG) simulations are sufficient to capture the antibodies' propensities to associate with membranes. The globally favored membrane-inserted Fab geometries agree across our multi-scale simulation stages and experiments. Extending CG trajectories into all-atom simulations facilitated building a thorough integrative model of bnAbs docking onto membranes to target Env. That is, bnAbs initially associate with a membrane surface, progress to a low energy CDR-embedded conformational ensemble wherein stable and specific CDR-mediated phospholipid complexes form, and then dynamically re-orient for MPER binding. Overall, the atomic simulations illuminate key molecular features that encode and tune each bnAbs'

range of preferred membrane-bound geometries. These molecular details include surprisingly important and underappreciated contributions from framework regions. To approximate membrane interaction strength of antibody models *in silico*, we benchmarked all-atom constant velocity pulling simulations in explicit lipid bilayers on 4E10 variants, successful differentiating experimentally determined differences in membrane binding affinity[21,25,28]. Finally, we tracked the membrane association strength of PGZL1 germline-reverted variants to mimic a pseudo-maturation pathway, demonstrating significant increase in lipid interactions as the antibody matures, which correlates with experimental neutralizing e fficacy[18].

We demonstrate the utility of this novel modeling framework to retrospectively study or potentially proactively engineer antibodies to better navigate the proposed 2-step bnAb neutralization mechanism and facilitate HIV vaccine design. Likewise, our results have broad implications for the *in vivo* selection of antibodies targeting membrane-embedded proteins. We expect the insights and approaches highlighted here to translate generally, beyond HIV, towards generalized principles for targeting membrane proteins at partially concealed juxtamembrane regions, which is highly desirable for therapeutic antibodies and vaccine design given the high protein sequence conservation often found near or within the membrane.

Atomic simulations accurately model interactions between MPER bnAbs and HIV-like lipid bilayers

To assess the stability, organization, and spectrum of phospholipid interactions inferred from previous lipid-bound crystallography and cryo-EM experiments for these bnAbs, we first performed unbiased all-atom simulations of 4E10, PGZL1, and 10E8 peripherally embedded to the surface of model lipid bilayers. Starting membrane-bound conformations for each Fab were computed using a structure-based docking method, PPM2.0[34], globally optimizing insertion using a per-residue solvation pseudo-energy based on residue hydrophobicity. All bnAbs were reasonably predicted with their CDR-H3 inserted into the membrane. Explicit solvent systems were built with simplified HIV-like anionic cholesterol-rich membranes (25% cholesterol, 5% 1-palmitoyl-2-oleoyl-sn-glycero-3-phosphate (POPA), 70% 1-palmitoyl-2. -oleoyl-sn-glycero-3-phosphocholine (POPC)), and four pseudo-replicate simulations of 1 microsecond (μs) each were initiated for each bnAb, with two replicates tilted by ±15 degrees to modestly vary the starting membrane-interacting pose.

In each pseudo-replicate simulation of each antibody, we observed one phospholipid to stably associate at a single site proximal to the Fab heavy-chain CDR loops (**Figures 1-2**). In some cases, phospholipid binding events formed very quickly, as early as the protein-restrained equilibration (15 ns) where lipids can freely diffuse (**Figure S1D,E**). Replicate simulations with artificially tilted Fab still robustly formed the CDR-mediated phospholipid complexes, usually after 50-250 ns of minor Fab reorientation on the membrane surface **(Supp. Video 1)**. These phospholipid binding events were highly stable, typically persisting for hundreds of nanoseconds. Across the three bnAbs, each respective CDR-phospholipid complex was present in >70% of the total aggregated 4 μs simulation time (**Figures 1C-D, 2B, S1D-F**). Time-averaged densities of the bound phospholipid atoms showed clear atomic overlap with electron density located at CDR sites within lipid-soaked X-ray structures wherein lipid headgroups were modelled (**Figures 1A-B, 2A, S1A-C**)[20,24,31]. Our simulations uncover the CDR-lipid interactions that are the most feasible and biologically relevant in the context of a full lipid bilayer. These results add validation to which out of the many possible ions and short-chain lipid moieties ordered within those crystal structures may be inferred as putative lipid. Notably, the loop backbone conformations for these CDRs remained internally rigid during the simulations (**Figure S2A,E,H**). Thus, these bnAbs constitutively present these pre-formed CDR binding sites for phospholipid loading at the bilayer surface upon insertion. In a PGZL1 simulation, we observed a lipid exchange event (**Figure S1E**), where a long-bound POPC molecule dissociated and was promptly replaced by a POPA molecule. Thus, while bound phospholipids are kinetically stable (~10^2 ns), they can freely associate and dissociate with CDR loops within the timescale of our simulations. Together, these behaviors indicate that phospholipids likely readily exchange at these CDR loop sites *in vivo* for membrane-associated bnAbs, with equilibrium strongly favoring the bound state. In summary, despite the different bnAbs mediating membrane interactions via distinct protein features, our simulations robustly and reproducibility capture the phospholipid binding process *ab inito* at experimentally determined CDR loop sites with atomic accuracy.

4E10 and PGZL1 are structurally homologous (85% sequence identity, sharing IGHV1-69 germline), both forming complexes at their CDR-H1 loop site predominantly coordinating via the lipid phosphate group[20,31,35]. Across 4E10 and PGZL1 simulations, the bound lipid phosphates were generally rigid within the CDR site (<0.75

Å RMSF), and maintained sub-atomic mean RMSDs relative to the reference position in X-ray structures: 0.6 and 0.7 Å, respectively (**Figure 1C-D, S2B,F)**. Likewise, the interactions coordinating the lipid phosphate oxygens at CDR-H1 were similar with atomic accuracy between MD simulations and the X-ray structures, with hydrogen bonds donated from Phe29 and Ser30 backbone amides and from Ser29/Thr29 and Ser30 sidechain hydroxyls[20,31] **(Figure 1A-B, S1A-B).** Although the headgroup phosphate displayed some positional dynamics and variation, this extensive polar network was mostly maintained over time – modestly fluctuating to accommodate the lipid.

These results of reliably recovering experimentally determined CDR-phospholipid complexes establish confidence that other antibody features in the simulation, namely the membrane-bound Fab conformation and ancillary protein-lipid interactions, are biologically relevant. Thus, we analyzed the additional molecular and sequence level features driving the lipid bilayer interactions. Time-averaged per-residue lipid interaction profiles separated by membrane layer (polar headgroup, glycerol, and hydrocarbon) show that 4E10 and PGZL1 heavy-chain loops were deeply immersed into the bilayer, whereas light-chains had sparse and only surface-level headgroup contacts (CDR-L1, -L2) **(Figure 1E-F)**. 4E10 CDR-H loops buried deeper into hydrocarbon chain layer of membrane and formed more extensive contacts with the lipid aliphatic tails compared to PGZL1 CDR-H loops. These patterns may in part explain 4E10's greater poly-reactivity. One striking and novel observation consistent between 4E10 and PGZL1 simulations was that heavy-chain framework region 3 (FR-H3) was extensively embedded, showing that surface features, which are predominantly germline encoded, contribute significantly to membrane binding and Fab orientation. Aligning interaction profiles with corresponding primary sequences for light-chain loops and FR-H3 reveals that charged residues mediate their shallower surface interactions **(Figure S3A-B)**, whereas the more deeply inserted CDR-H loops bare neighboring stretches of hydrophobic and lipophilic polar residues. These analyses supply comprehensive atomic-detail maps of bnAb-membrane interfaces. Delineating the molecular features defining these protein-lipid surfaces adds key context to complement the battery of previous experiments characterizing the insertion, accessibility, and relative orientation of the MPER epitope with and without bnAbs – additionally highlighting contributions from framework regions to membrane interaction previously underestimated.

We similarly investigated bnAb 10E8, which differs in its genetic origins and expected light-chain-mediated membrane binding mode. In all 4 replicate simulations, we observed a POPC complexed at a groove between CDR-L1 and FR-L3 which had had significant non-protein electron density in previous 10E8 X-ray structures with and without lipids **(Figures 2A-B, S1C,F)**, modelled as headgroup phosphoglycerol anions, glycerol, or free dihydrogen phosphate. In our simulations, the POPC phosphate was slightly offset (2.7 Å) from the proposed CDR-L1 crystallographic site, instead complexing mainly with FR-L3 stabilized by a hydrogen bonding network from Ser83 hydroxyl, Gly84 backbone amide, and Asn85 C-alpha proton **(Figures 2A, S1C)**. In parallel, a POPC choline moiety simultaneously occupied the CDR-L1 site, paring the choline cation with four carbonyls from the CDR-L1 backbone due to its short helical conformation **(Figure 2B)**. Thus, our simulation finds stable bivalent complexes at this CDR-L1 FR-L3 groove with the lipid phosphocholine (PC) zwitterion with >70% occupancy overall across replicate simulations (CDR-L1–choline site RMSF = 0.5 Å; FR-L3–phosphate site RMSF = 0.5 Å). These 10E8 loops were also conformationally rigid (RMSF < 1.0 Å, **Figure S2H**), presenting a pre-formed binding site. The bilayer in our simulations provides a more realistic and contextualized environment to model these interactions compared to lipid-soaked X-ray crystallography structures, where lipids have unlimited degrees of freedom to access loops. This CDR-L1 site highlights the importance of phospholipid binding features at CDR-L1 in the 10E8 binding and neutralization mechanism, given that the double mutant of R29 and Y32 to alanine exhibited vastly decreased neutralization (>500 fold) across HIV strains[24].

Additionally, we sought to assess the biological relevance and *in silico* predictability of these observed CDR-lipid polar interactions using an orthogonal bioinformatics approach. We mined protein-ligand interactions to assessed whether phosphate complexes of similar geometries have been observed in nature, positing that the occurrence of analogous phosphate interactions outside the context of MPER bnAbs, i.e. within critical structural or functional regions of other protein families, can differentiate common proteome-wide functional motifs from simulation artifacts. Structural searches querying the lipid-binding loop backbone conformation of each Fab (as previously described[14,20,24]) identified between 10^5 to $2{\cdot}10^6$ geometrically similar sub-segments within natural proteins (<2 Å RMSD)[37], highlighting their prevalence in the protein universe. These hits were subsequently mined for nearby phosphate/phosphoryl and sulfate/sulfo ligands **(Figure S4)**. Only 4 cases of phosphate-type

ligand binding motifs were identified when searching structures similar to 4E10's and PGZL1's CDR-H1. As such, this CDR-H1 site is a realistic but rare protein-phospho-ligand structural motif (**Figure S4A,B**; **Table S1**). For 10E8's CDR-L1 site, only 1 phosphate-type ligand was observed: a solvent-exposed surface crystallographic ion. By contrast, 10E8's FR-L3 beta-turn site was a hot spot for phosphate-type ligands, with 23 natural protein cases **(Figure S4C, Table S1)**. Thus, while both CDR-L1 and FR-L3 10E8 loops sites can bind phosphate ligands, the much greater natural prevalence of phosphates ligated at FR-L3 supports that the 10E8 bivalent POPC complex in our simulations is a biologically realistic site. Barring experimental validation, existence of this FR-L3 site establishes precedent for how important framework regions can be for mediating protein-membrane interactions, including hosting stable and specific phospholipid complexes.

Next, we examined the geometries of the membrane-bound conformational ensembles sampled in 10E8, 4E10, and PGZL1 simulations, given the emphasis on tilt of the antigen-antibody complex relative to the bilayer in proposed mechanisms of neutralization[30] and the potential energetic cost, if any, for reorienting to facilitate MPER access and complex with Env. Fab conformations were described by the immersion depths of each CDR loop and 2 angles relating the global domain orientation to the membrane. Structural clustering distinguished micro- and macroscopic sub-states sampled globally and individually **(Figure S5A-C)**, with 6 or 7 relatively well-distributed micro-states for each bnAb (5 – 30 % population fractions) describing the spectrum of surface-bound conformations **(Figure S4D,F,G)**. Interestingly, while all 4E10 micro-states maintain 86-98% occupancy of the CDR-H1 phospholipid complex, 10E8 and PGZL1 microstates showed more variance in propensity to form CDR-phospholipid complexes **(Figure S5E,G,I)**. Namely, two of 10E8's micro-states had low CDR-L1 PC headgroup occupancy (23% and 33%), while two other micro-states were bound in 83% and 78% of frames, respectively. Thus, formation and maintenance of key phospholipid complexes can depend on the CDR and FR binding site loop orientation and accessibility at the bilayer headgroup sector, highlighting the importance each bnAbs' characteristic surface-bound conformational ensemble upon association and the protein sequence features mediating these geometries.

We next studied bnAb LN01, previously crystallized with a minimal MPER fragment as well as an extended TM-MPER fragment, to interrogate differences in the antibody surface-bound conformational ensemble

in the context of a transmembrane antigen **(Figure 3A,C)**[19]. These MPER-bound LN01 structures also included ordered detergent and phospholipids, and suggest two putative relevant CDR-phospholipid binding sites. Site one occurs at an CDR-H3-L1-L2 inter-chain groove, coordinating a PC headgroup via a CDR-L1 Lys31 salt bridge to the lipid phosphate and engages the choline with CDR-L1 Tyr32 and CDRH3Tyr100g in a cation-pi cage motif – optionally including the MPER epitope helix Trp680 and Tyr681 aromatics **(Figures 3E,G, S1G)**. The more solvent-exposed second site between CDR-H1 and -H2 binds phosphatidylserine (PS) or PC headgroups. In replicate half-μs simulations for both LN01 alone and the LN01-MPER-TM complex in HIV-like model membranes, several POPC binding events were observed at the CDR-H3-L1-L2 groove. The headgroup polar atom positioning in LN01's sidechain interaction network was reproducibly recovered with atomic accuracy versus ordered dodecyl-PC to X-ray structures (**Figure 3E-H)**. However, compared with PGZL1, 4E10, and 10E8 simulations, the kinetic stability and occupancy for phospholipids in LN01 at the CDR-H3-L1-L2 groove site were much lower ~30% and ~40% phospholipid-bound overall for LN01-MPER-TM and apo, respectively (**Figures 3I-J, S1H-I)**. The second crystallographic CDR-H1-H2 PS/PC site was not recovered in any replicate simulation.

Two novel features stood out in LN01 simulations. First, antigen-free LN01 sampled a broader breadth of geometries at the membrane surface, characterized by two angles describing the Fab relative to the membrane (**Figure 3A-D**). LN01 was more deeply and extensively embedded when complexed with MPER-TM than LN01 alone. The more focused conformation landscape likely resulted from the Fab accommodating the inserted MPER-TM antigen's lowest energy orientation. Comparing the per-residue protein-lipid interaction profiles revealed consistency in the protein molecular features mediating membrane association **(Figure 3K-L)**, although CDR-L, CDR-H, and FR-L3 loops were inserted further upon TM antigen engagement. While the MPER-TM fragment may present the epitope differently than the full length Env trimer, our data describe how a bnAb shifts its global geometry to access and engage a transmembrane-presented MPER; yet, the apo state is predisposed based on CDR loop insertion and samples this geometry readily within its resting conformational ensemble on the membrane surface. Then, the bnAbs' sequence and structure are primed for transmembrane epitope engagement.

The second notable feature was an additional LN01 CDR-phospholipid binding site predicted across simulation replicates at an alternative groove comprised of CDR-H3, FR-L2, and CDR-H2. We named this the "Loading site" given its proximity (~7 Å) to the previously observed CDR-phospholipid H3-L1-L2 "X-ray" site and observations that phospholipids quickly exchange from the Loading site into the X-ray site by diffusion **(Figure S1H,I)**. Although, the two sites were often simultaneously occupied by distinct lipids. Similar to the X-ray site, Loading site binds lipids in the apo state, but in the presence of the MPER-TM can optionally including antigen TM residue Trp680 (**Figures 3F,H,I-J, S1G**). LN01 Tyr100g, Tyr49, and Tyr52 (and gp41's Trp680 in MPER-TM-bound simulations) hydrogen bond with the lipid headgroup phosphate oxygens. The POPC choline is simultaneously engaged by electrostatic contacts from Tyr49, Tyr52, Thr53, Thr100c, Ser100d, and Tyr100g side chains, forming second cation-pi cage motif structurally analogous to that used at the X-ray site **(Figure 3E-H)**. The Loading site was occupied an average of 78% of LN01-MPER-TM simulation time versus 58% for apo LN01 replicates **(Figures 3I,J S1H,I)**. Thus, these LN01 simulations highlight that the paratope-epitope-membrane complex robustly reforms and is stable in the lipid bilayer context. The ternary complex also may incorporate multiple phospholipid participants loaded prior to epitope engagement, which add stabilizing interactions with the MPER helix. These results strengthen the argument that antibodies can evolve structural elements to engage both a membrane protein antigen and the surrounding lipid environment – and that we can predict as well as possibly engineer these molecular features *in silico*.

Coarse-grain *ab initio* insertion simulations capture biologically relevant membrane-bound conformations

Because the limited sampling accessible in all-atom simulations, we turned to coarse-grained (CG) simulations utilizing the Martini model to explore the process of antibody insertion to lipid bilayers and more thoroughly assess the range of plausible and favorable bnAb surface-bound geometries. With elastic network restraints, CG representation was structurally stable in simulations, maintaining Fab tertiary and quaternary structure (<2 Å backbone RMSD, **Figure S6A**). Then, we hypothesized that this simulation model, which rigidly presents Fabs' macroscopic surface features (hydrophobic patches, charged patches, polarity) as polar beads,

would be sufficient to capture these bnAbs' preference for membrane insertion and their rough geometric preferences.

We developed two CG simulation methods to probe the association process. In the first approach termed "spontaneous insertion", 18 simulation replicates were initiated with the Fab placed in water at different random initial orientations and distances (0.5 – 2 nm) above a pre-assembled HIV-like anionic lipid bilayer, wherein the protein could freely diffuse for 14 µs **(Figure 4A)**. For 4E10, PGZL1, and 10E8, most replicates contacted the membrane and stably inserted for longer than 1 µs; 10, 14, and 12 extended insertion events were captured respectively (**Figure 4B-D, Table S2**). The simulations also captured both dissociation events and preliminary scanning behaviors, indicating the reversibility and dynamics of the process. As a reference, bovine serum albumin (BSA) was tested similarly. Its documented weak affinity for lipid bilayer association (low millimolar) aligns well with the vastly reduced number of membrane contact events (2/18), minimal overall contact time, and lack of sustained insertion observed **(Figure 4E)**. We also tested 13h11, a non-neutralizing anti-gp41 antibody experimentally shown to have undetectably low lipid bilayer interaction[7,40], as a more relevant control to antibody-based features (**Figure 4E**). 13h11 exhibited negligible insertion and only sparse short 'scanning' events. Thus, these CG simulations readily distinguish MPER bnAbs with high propensity for lipid interaction (low micromolar affinity) from non-specific and low affinity lipid interactions.

As an alternative strategy to sample bnAbs insertion and favored geometries, we developed a "co-assembly" CG simulation. Each simulation box hosted one Fab at a varied initial orientation amongst a mixture of randomly placed water, ion, and lipid particles as a starting point for subsequent unrestrained MD, leading to spontaneous assembly of the lipid bilayer – often yielding Fab membrane insertion (**Figure 4F**). This approach increased predisposition for Fab-lipid interactions and reduced wasted time sampling Fab diffusing in bulk water, successfully resulting in more trajectories with Fab inserted in distinct geometries and overall membrane contact time **(Figure 4G-I, 5B)**. However, this method also risks enriching insertion in less favorable states, possibly skewing the conformational distribution. We combated these biases by running more replicates (n=40) of shorter 5 µs simulations. Fab dissociation was also readily observed from initially inserted or 'scanning' trajectories,

suggesting that coarse-grained models can distinguishing unfavorable and favorable membrane-bound conformations.

Next, we characterized the spectrum of membrane-bound conformations sampled the two CG approaches for each bnAb and compared with our pre-inserted all-atom simulations. We tracked the global Fab domain orientation through the canonical "angle of approach" (angle of the Fab' long axis relative to the membrane normal vector) alongside a second "rotation angle" tracking Fab rotation around its long axis **(Figure 5A)**. Both CG approaches significantly sampled conformations analogous to the primary state adopted in all-atom trajectories for each bnAb, although with a broader local geometric distribution. Interestingly, PGZL1 and 10E8 heavily sampled alternative membrane-inserted conformations, while 4E10 inserted only in a single conformation. It is unclear whether this observed conformational specificity represents a deeper energy well for 4E10's primary geometry or is due to the Martini model over-estimating hydrophobic interactions[41].

Notably, all membrane-associated conformations are mediated by CDR interactions across bnAb systems **(Figure S6C-E)**. Overall, many macroscopic states sampled appear to be biologically relevant, given their geometric similarity with all-atom conformations shown to stably bind phospholipids. For 10E8, spontaneous insertion performed better at sampling geometries akin to those observed in all-atom simulations. Geometries that 4E10 and PGZL1 sampled in co-assembly trajectories overlapped more with all-atom simulations. Nonetheless, we show CG Fab representation can be useful for investigating dynamics of insertion and landscape of surface-bound conformations.

Integrative multi-scale simulations of *ab initio* formation of bnAb phospholipid complexes

We then tested whether the full process of bnAb association followed by formation of specific phospholipid complexes could be modelled *ab initio* by integrating spontaneously inserted CG conformations into all-atom trajectories. These simulations assessed compatibility of CG-derived surface geometries to form those specific headgroup interactions, barring minor geometric reorientation. Medoid Fab poses for each of 4E10, PGZl1, and 10E8 were extracted representing 3 structural distinct states after clustering CG simulation frames (subsets A, B, C), then converted to all-atom detail for unbiased MD simulation (**Figure 6A-B**).

For 4E10, trajectories initiated from all three geometries spent extended time (>100 ns) with phospholipid bound at the CDR-H1 site (**Figure 6E**). These trajectories also drifted back to conformations similar to those in our previous pre-inserted all-atom simulations as measured by the global angles sampled (approach angle, 60-80°; **Figure 6C**) and per-residue interaction profile (CDR-H2-H3 insertion, **Figure 6D**). Back-mapped trajectory A was distinguished by deeper insertion, with the highest >60% CDR-H1 phospholipid binding occupancy (>60%), and the most resemblance to our previous atomic simulations (**Figures 1E, 6D**). Trajectories initiated from clusters B and C are slightly tilted (rotation angle > 0°) and less extensively inserted, exhibiting lower CDR-H1 phospholipid occupancy (**Figure 6C-E**). Thus, these integrative 4E10 simulations show how CG simulations could be used to generate stable membrane-bound conformations that align with laboratory experiments and capture the specific phospholipid binding events crucial for bnAbs function – all totally *ab initio*.

Similarly, for PGZL1, all-atom trajectories starting from CG clusters B and C conformationally converge to similar CDR-H-inserted geometries sampled in previous all-atom MD, and stably bind phospholipid headgroups at CDR-H1 (>50% occupancy) **(Figure 6C-E)**. However, for the trajectory initiation from cluster A, a novel membrane-bound conformation is sampled, which is similarly mediated by CDR-H3 insertion but now supplemented with light-chain contacts. No CDR-H1 lipid complex is detected. This exploration of the additional membrane-bound geometries facilitated by CG sampling highlights alternative kinetically stable states, which may represent modeling artifacts or may capture relevant intermediate conformations aiding membrane association (e.g. preliminary surface-scanning).

10E8 back mapping revealed advantages as well as limitations in the spontaneous insertion CG method. The all-atom trajectory from a CG cluster A initiated from an alternative conformation (approach angle, ~20°; rotation angle, ~55°) rapidly dissociated from the membrane within 100 ns. This instability indicates the conformation is likely an artifact, despite being a predominant geometry in CG simulations **(Figure 6B,C)**. Interestingly, the all-atom trajectory starting from CG cluster B trended towards the same novel conformation as cluster A, but remained stably inserted, albeit having shallower CDR-H3 insertion alongside canonical 10E8 CDR-L embedding **(Figure 6C-D)**. Cluster C started and finished in membrane bound orientations most similar to our previous atomistic simulations (**Figure 6C**), although with a slightly different protein-lipid interaction pattern **(Figure 6D**).

Curiously, the bivalent CDR-L1 FR-L3 phospholipid complex could still be formed with high occupancy for both cluster B and C (>70%, **Figure 6E).**

We evaluated the possibility of a bivalent IgG interaction with the membrane to provide further mechanistic context with the physiologically relevant molecular structure. Aligning a full-length IgG onto extracted membrane bound Fab conformations suggests it is unlikely that two Fabs simultaneously engage the membrane via low energy conformations due to rotational strain on the IgG hinge region **(Figure S7E-F)**. Together, these integrative modeling data in concert reflect both the value added and the caveats from additional sampling of membrane-bound bnAb conformations from CG trajectories. This *ab initio* multi-scale simulation approach can identify bnAbs' apparent lowest energy state with high occupancy CDR-phospholipid complexes. Additionally, sampling a broader range of bnAb surface geometries revealed a wider range of conformations are compatible with forming each bnAb CDR-phospholipid complex, although often with lower occupancy and stability. However, many heavily sampled CG states are likely simulation artifacts and biologically irrelevant, indicated by dissociation or poor insertion patterns upon simulation at atomistic detail. Nonetheless, we demonstrate the utility of this integrative approach for unbiased investigation of the dynamic process of insertion, mapping antibody-membrane interactions, and detecting specific phospholipid binding *ab initio* at atomic detail.

Atomistic pulling simulations distinguish differences in affinities of experimentally characterized variants

Having established these workflows, we sought to gain a more quantitative energetic view of how these membrane-bound conformations and lipid interactions connect with physiological properties such as affinity and neutralization. Canonical free energy calculations at atomic-detail (e.g. potential of mean force, P.M.F.) requires simulation timescales (10's of μs)[42] prohibitive for characterizing more than a few antibody variants. Here, we developed a more expedient approach, applying constant velocity biased all-atom simulations to determine the rupture force required to dissociate a Fab bound to lipid bilayers. This method provides a binding strength estimate akin to force spectroscopy **(Figure 7A**). Given that Fabs can sample many lipid interactions and surface

conformations, we performed ensemble-based measurements: averaging forces from several replicates of pulling trajectories each initiated with different starting configurations (which were extracted from unbiased MD).

First, to assess suitable pulling velocities, we began dissociating 4E10 from simplified anionic HIV-like lipid bilayers to a fixed distance (1.5 nm) along the membrane normal over different time spans (10, 50, 100, 200 ns), initiating 3 replicates from unique starting conformations (**Figure S7A-B**). Interestingly, 2 of 3 initial Fab models at their CDR-H3 W-W motif adopt a rotameric state where Trp100a remains inserted in both states but Trp100b projects down towards lipid tails in the "Trp-Down" state while in the other model Trp100b is flipped up towards the lipid-water interface ("Trp-Up" state). As expected, rupture forces decrease with increasing simulation time (slower pulling velocity), plateauing between 100 and 200 ns (**Figure S7A**). Surprisingly, the rupture force was nearly identical (< 2% difference) between the two Trp-Down pulling trajectories at both 50 ns and 100 ns (78.5 and 56.2 kJ/mol·nm^2, respectively), and was consistently higher than forces from the Trp-Up conformation (27 and 47% greater, respectively) (**Figure S7A**). This cursory trial of bnAb dissociation force calculations exhibited promising conformational sensitivity in distinguishing different CDR loop protein-lipid interactions and remarkable precision between similar starting Fab conformations.

We next benchmarked this technique by comparing behavior of 4E10 with its well-studied WAWA variant (W100aA-W100bA CDR-H3 mutant) (**Figure 7B**). WAWA fragments have similar K_d to MPER antigens, but significantly reduced affinity to HIV-like empty liposomes and drastically reduced neutralization efficacy (>100 fold higher IC_{50})[21,25,28,43]. Thus, we hypothesized that *in silico* estimation could assist in making the molecular link between WAWA's reduced membrane binding and defective neutralization. Across replicates from different starting membrane-inserted conformations for 4E10 (n=9) and WAWA (n=11), rupture force calculations showed average forces (± S.E.M.) of 63.8 ± 2.8 kJ/mol·nm^2 and 48.0 ± 2.6 kJ/mol·nm^2 respectively (**Figures 7D-E, S7D**), correctly indicating the 4E10 ensemble has a much stronger membrane interaction (32 ± 13 %; p-value < 0.001). Thus, this ensemble analysis approach robustly discerned antibodies of high (~1 μM) and low membrane affinity previous measured experimentally and should prove useful in investigating the apparent correlations between bnAb molecular features, lipid bilayer interactions, and neutralization potency. Notably, each simulation set

required 30-40 hours (replicates in parallel) in a modern computing environment, which is less than 10% needed for a PMF[42] and reflects medium throughout scalable to hundreds of antibodies per year.

Finally, we evaluated the membrane interactions of experimentally characterized PGZL1 variants that recapitulate possible stages of a germline maturation pathway[20] (**Figure 7C**). Mature PGZL1 has relatively high affinity to the epitope peptide (K_d = 10 μM) and demonstrates great breadth and potency, neutralizing 84% of a 130 strain panel. An "Intermediate" PGZL1 with V-gene germline reversion (gVmDmJ, having CDR-H3 100% sequence identity, **Figure S7D**) showed a modest reduction in affinity (K_d = 64 μM), but greatly reduced neutralization potency and breadth (12% of 130 strains)[20]. The loss of neutralization efficacy is far greater than expected from the modestly lowered antigen affinity alone, and was hypothesized to be due to vastly reduced propensity for lipid interactions of this variant[20]. The completely reverted "Germline" version (gVgDgM) had no detectable MPER affinity or neutralization. To predict the initial membrane-docked Germline and Intermediate Fab models, we performed the aforementioned unrestrained all-atom workflow starting with hydrophobicity-optimized inserted conformations. The PGZL1 Fabs all had similar predicted insertion geometries, facilitated by long and relatively hydrophobic CDR-H3 conserved across variants **(Figure S7D)**. CDR-H1-phospholipid complexes were not formed during Intermediate or Germline unbiased simulation.

Ten unique lipid-inserted conformations were extracted from the MD ensemble to initiate replicates of biased membrane dissociation simulations. Significantly lower forces were required to dissociate Intermediate and Germline PGZL1 from bilayers, 37.5 ± 14.9 kJ/mol·nm^2 and 41.2 ± 11.7 kJ/mol·nm^2 respectively, than for mature PGZL1, 56.1 ± 11.6 kJ/mol·nm^2 ($p < 0.003$) **(Figure 7E)**. The Germline PGZL1 likely represents a kinetically stable but low affinity interaction, setting the low baseline of rupture forces required to dissociate CDR-inserted antibodies. While the difference in Germline and Intermediate force distributions was not significantly different ($p > 0.4$), more higher force events were observed for the Intermediate variant versus Germline. Thus, PGZL1 more favorably interacts with anionic HIV-like membranes than inferred maturation pathway precursors. We did not disentangle the energetic contributions to membrane affinity of the CDR-H1 phospholipid complex from other protein-lipid interactions determining mature PGZL1's enhanced membrane interaction here, but the roles of these features should be explored in future work. These results provide evidence

that phospholipid binding features are acquired and honed along a bnAb maturation pathway, entrenching the molecular link between positive selection of bnAb lipid binding properties and acquiring neutralization efficacy.

Discussion

Here, we present a roadmap for applying integrative molecular simulations to characterize the biophysical underpinning of lipid membrane interactions within the mechanism of HIV MPER bnAbs. The methods developed and principles extracted improve understanding of maturation pathways for antibodies targeting membrane-proximal epitopes and should enrich data-driven design of HIV immunogens. Our detailed simulations supplement *in vitro* binding and crystallographic evidence in demonstrating that bnAbs develop highly specific phospholipid interactions that facilitate access to the MPER epitope and can participate in epitope-paratope interface in context of full lipid bilayers. Furthermore, the modeling approaches demonstrated here could be used both retrospectively or proactively: to identify, characterize, and even engineer membrane-targeting elements in antibodies.

Further, these simulations can serve future examination of molecular details concerning the genetic origins and developmental pathways for incipient lipid-binding antibodies. Through natural or vaccine-induced immunity, coaxing the immune system to develop both lipid and antigen affinity (possibly even cooperativity) during maturation is a difficult task, and hindered by downregulation of membrane binding precursors[1,3,6,11]. Likewise, MPER bnAbs are difficult to induce and have only been isolated from patients with chronic HIV-infection and sustained immunosuppression[17,18,35,43,44]. Modern vaccine strategies often elicit certain subsets of precursor B cells, often targeting specific germline genes, in attempt to guide antibodies' mature of specific molecular features intended for the targeted epitopes[45,46]. The question remains whether particular germline genes and lineages are privileged for successful maturation as membrane-targeting (or MPER-targeting) antibodies. This notion is supported by 4E10 and PGZL1, which share a germline gene (VH1-69)[20] and demonstrate near identical membrane interactions. To this end, germlines genes with inherent basal membrane affinity may be favored as MPER bnAb precursors, potentially circumventing auto-immune checkpoints during maturation or presenting unique scaffolds compatible with further evolution of lipid binding properties. Specific CDR lipid-

binding motifs are predicted to be encoded early in maturation processes for PGZL1[20], namely the CDR-H1 loop **(Figure S7D)**. These features are complemented by mutated membrane contacting residues in the FR-H3 surface and CDR-H3 loop, which are incorporated later in the maturation process **(Figure S7D)**. Across MPER bnAbs, membrane-binding features are likely acquired at strategic timepoints throughput development to balance poly-specificity and evade autoimmune checkpoints[47]. Experimental databases of germlines genes usage and of B-cell repertoires sequenced during immunization courses would be ideally paired with the simulations described here to investigate *in vivo* filtering of lineages with lipid-binding variants and assess possible rules of the autoimmune system[48].

Beyond gp41-targeting antibodies and lipid antibodies in autoinflammatory diseases[49,50] or microbial infections[51,52], we suspect a broader scope of positive outcomes from antibody tolerance and interaction with lipid bilayers may occur in Nature and is currently underestimated and underutilized. Although host cross-specificity of 4E10 is well documented, the vastly reduced poly-reactivity of PGZL1 and 10E8 inspires optimism that maturation of phospholipid interactions and membrane tolerance may be viable to incorporate into emerging vaccine design strategies and therapeutic antibodies for other membrane proteins to facilitate access of conserved, buries epitopes[33]. Currently, the breadth of analogous antibodies targeting membrane protein while making extensive or cooperative lipid interactions is poorly explored. The simulation procedures and principles described here are well positioned to investigate this outstanding question and could help define broader chemical rules for design of membrane-interfacing antibodies.

Acknowledgments

The authors would like to acknowledge the High-Performance Computing Core at Scripps Research, particularly JC Ducom. Michael B. Zwick provided inspiration and helpful discussions. C.A.M. was supported by the John and Susan Diekman Skaggs Graduate School Fellowship. This work was funded in part by Cooperative Agreement award UM1 AI144462 in partnership with the Division of AIDS, NIAID [I.A.W. and A.B.W.].

Author contributions

C.A.M. and M.M. performed the MD simulations and conceived of the methodology. C.A.M. quantitatively analyzed the MD simulations. J.G. and C.A.M. conducted the structural bioinformatics analysis. C.A.M., I.A.W., A.B.W., and M.M. designed the experiments, analyzed the data, and wrote the manuscript with input from all authors.

Declaration of interests

The authors declare no conflicting interests.

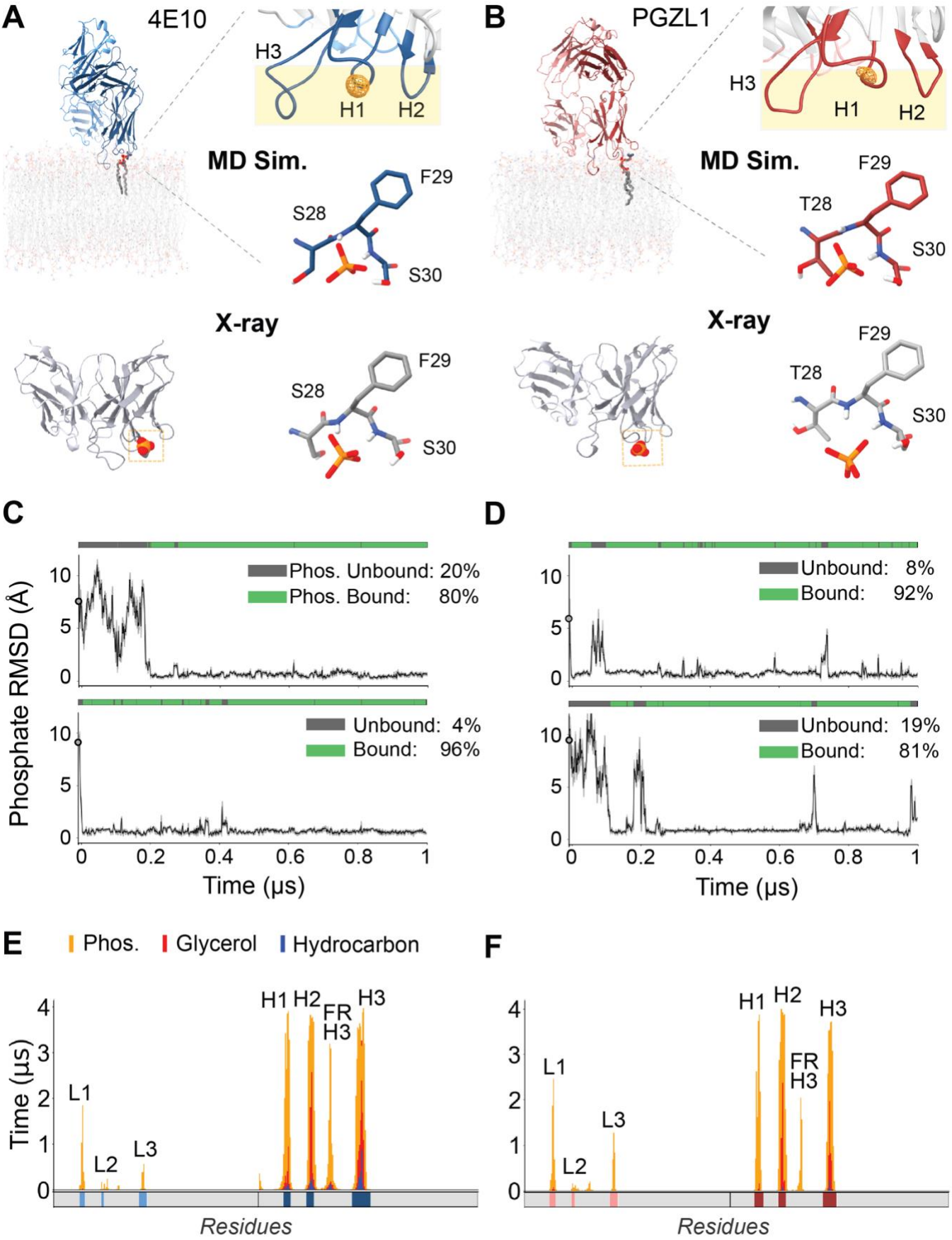
A
4E10
H3
H1
H2
MD Sim.
F29
S28
S30
X-ray
F29
S28
S30
B
PGZL1
H3
H1
H2
MD Sim.
F29
T28
S30
X-ray
F29
T28
S30
C
Phosphate RMSD (Å)
Phos. Unbound: 20%
Phos. Bound: 80%
Unbound: 4%
Bound: 96%
Time (μs)
D
Unbound: 8%
Bound: 92%
Unbound: 19%
Bound: 81%
Time (μs)
E
Phos.
Glycerol
Hydrocarbon
Time (μs)
L1
L2
L3
H1
H2
FR
H3
H3
Residues
F
L1
L2
L3
H1
H2
FR
H3
H3
Residues

Figure 1. 4E10 and PGZL1 CDR lipid phosphate binding sites and membrane interaction profiles in all-atom fluid HIV-like bilayer MD simulations

(A) Representative frame from an MD simulation of the phospholipid complex at 4E10 Fab CDR-H1 (top left). Top right, time-averaged lipid phosphate density (orange mesh) relative to antibody CDR loops embedded in the bilayer (beige) from 4 µs total time (top right). Center right, CDR-H1 loop side chain and backbone atoms of *de novo* predicted phosphate interaction (middle right). Bottom, putative lipid phosphate binding site observed in an X-ray structure for 4E10 (PDB: 4XC1), comparing the CDR-H1 loop interactions to MD (bottom right).

(B) PGZL1 lipid phosphate interaction at the CDR-H1 loop from MD simulation versus X-ray crystallography (PDB: 6O3J), demarked as in (**A**).

(C) RMSD of the interacting lipid phosphate versus the experimental CDR-phosphate position (X-ray site), classified as bound (green) and unbound (grey) by loop-phosphate contacts in 2 4E10 representative replicate trajectories. Black line, ten-frame RMSD running average; standard deviation, grey shading.

(D) RMSD of lipid phosphate binding to PGZL1 CDR-H1 in MD simulations versus X-ray site.

(E) Per-residue interaction profiles for Fab simulations of 4E10 detailing the time spent for each residue in in phosphate layer (orange), glycerol layer (red), or hydrocarbon layer (blue) across aggregate 4 µs from 4 simulations. CDR loops are mapped in solid color blocks below each profile, and Fab domain regions making significant contact are labeled.

(F) Per-residue interaction profiles for antibody Fab simulations for PGZL1, colored as in (**E**).

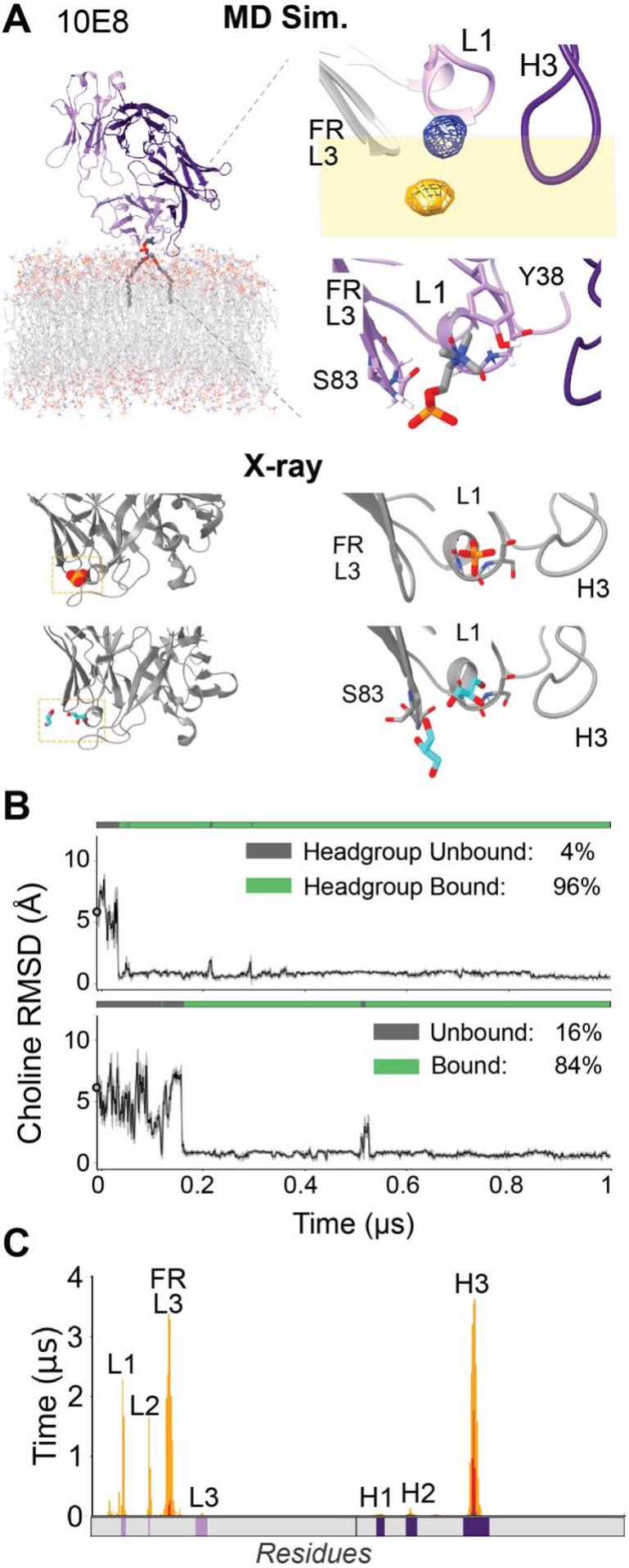
A
10E8
MD Sim.
L1
H3
FR
L3
FR
L3
L1
Y38
S83
X-ray
L1
FR
L3
H3
L1
S83
H3
B
Headgroup Unbound: 4%
Headgroup Bound: 96%
Unbound: 16%
Bound: 84%
Choline RMSD (Å)
Time (μs)
C
Time (μs)
FR
L3
H3
L1
L2
L3
H1
H2
Residues

Figure 2. 10E8 bivalent lipid headgroup interaction and bilayer insertion predicted in MD simulation closely matches experimental lipid binding sites

(A) Top left, representative frame from MD simulation of lipid interacting with 10E8 Fab. Top right, the MD lipid binding site includes a bivalent choline and phosphate lipid headgroup complex (represented as blue and orange mesh time-averaged positional density in simulations) within a protein surface groove composed of CDR-L1 and FR-L3 respectively. Bottom, positions of phosphates or glycerols modeled at the CDR-L1 and FR-L3 groove site within 10E8 Fab X-ray structures (PDB: 5T85, 5T6L)

(B) RMSD of lipid choline position in the MD simulations versus expected CDR-L1 lipid binding site from 10E8 X-ray structures. "Bound" state assigned relative to choline position and phosphate FR-L3 interactions observed in MD.

(C) Per-residue interaction profiles for antibody Fab simulations for 10E8, colored as in Figure 1E.

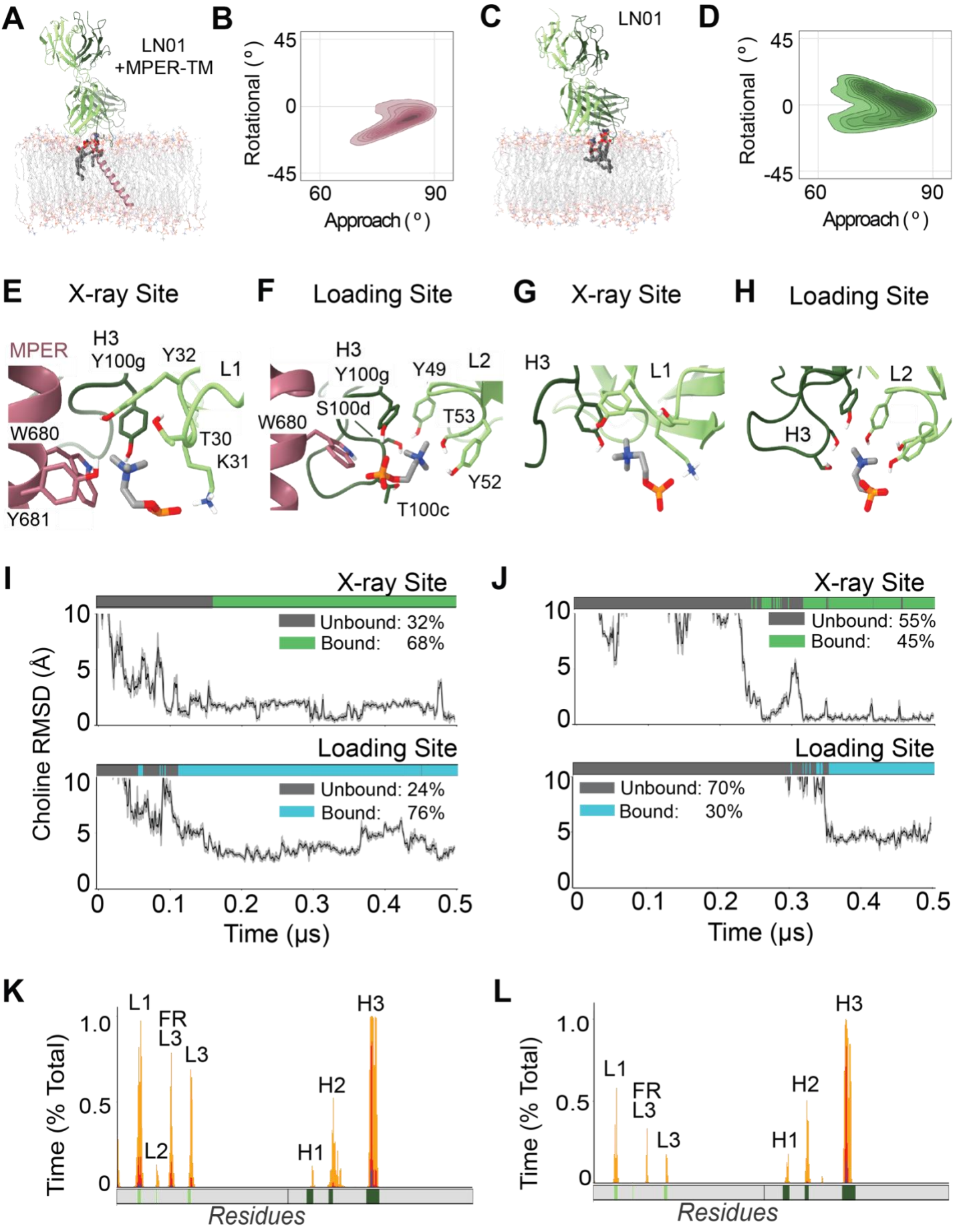
A
LN01
+MPER-TM
B
Rotational (°)
45
0
-45
60
90
Approach (°)
C
LN01
D
Rotational (°)
45
0
-45
60
90
Approach (°)
E
X-ray Site
MPER
H3
Y100g
Y32
L1
W680
T30
K31
Y681
F
Loading Site
H3
Y100g
Y49
L2
S100d
W680
T53
Y52
T100c
G
X-ray Site
H3
L1
H
Loading Site
L2
H3
I
X-ray Site
Unbound: 32%
Bound: 68%
Loading Site
Unbound: 24%
Bound: 76%
Choline RMSD (Å)
10
5
0
0
0.1
0.2
0.3
0.4
0.5
Time (μs)
J
X-ray Site
Unbound: 55%
Bound: 45%
Loading Site
Unbound: 70%
Bound: 30%
10
5
0
0
0.1
0.2
0.3
0.4
0.5
Time (μs)
K
Time (% Total)
1.0
0.5
0
L1
FR
L3
L3
L2
H1
H2
H3
Residues
L
Time (% Total)
1.0
0.5
0
L1
FR
L3
L3
H1
H2
H3
Residues

Figure 3. Atomistic simulations of apo and antigen-bound LN01 characterizing paratope-phospholipid complexes with and without epitope and shifted membrane-bound conformation

- **(A)** Representative frame from MD simulation LN01 Fab bound to MPER-TM showing the stable ternary paratope-epitope-membrane complex; bound phospholipids shown.
- **(B)** Frequency of Fab's characteristic surface-bound geometry by global domain rotation and approach angles in MD simulations for LN01 bound to MPER-TM, plotted by kernel density estimation as contour.
- **(C)** Representative frame from MD simulation of phospholipids complexed with LN01 Fab alone.
- **(D)** Frequency of geometries sampled for apo membrane-bound LN01.
- **(E)** Phospholipid headgroup interaction formed *ab initio* in LN01+MPER-TM simulations. Aromatic cation-pi cage motifs coordinate choline while the phosphate is coordinating by Lys31 matching the X-ray site binding pose.
- **(F)** The additional distal "Loading" phospholipid site predicted in LN01simulations, with a similar cation-pi cage motif and hydrogen bonds interactions stabilizing the PC headgroup.
- **(G)** Atomic interactions at the X-ray site in apo LN01 simulations.
- **(H)** Interactions at the loading site in apo LN01 simulations.
- **(I)** Lipid headgroup binding in representative simulation of LN01+MPER-TM (n=4 total). Top, X-ray binding site occupancy (green) and phospholipid choline RMSD in a representative trajectory versus experimental position. Bottom, loading site occupancy (cyan) and choline RMSD versus average headgroup bound position.
- **(J)** Lipid headgroup binding for representative apo LN01 trajectory (n=4 total). Site occupancy and RMSD versus predicted binding position for X-ray site (top) and loading site (bottom).
- **(K)** Per-residue interaction profile for MPER-TM-bound LN01.
- **(L)** Per-residue interaction profile for apo LN01.

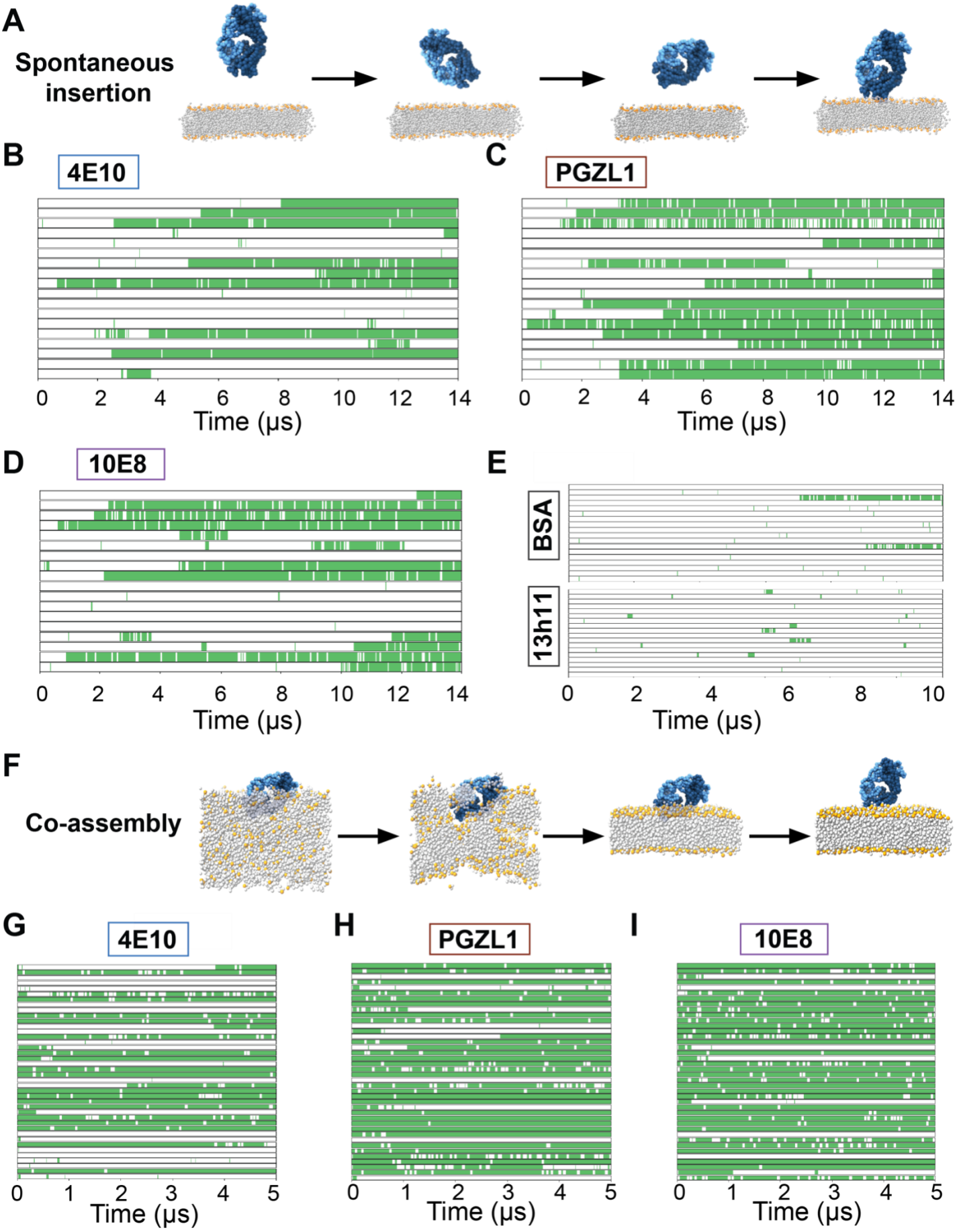
A
Spontaneous insertion
B
4E10
C
PGZL1
D
10E8
E
BSA
13h11
F
Co-assembly
G
4E10
H
PGZL1
I
10E8
Time (μs)

Figure 4. Unbiased spontaneous membrane insertion events and semi-biased dissociation events in coarse grain MD simulations

(A) Snapshots of spontaneous insertion event from a Martini model coarse-grain simulation of a 4E10 Fab. The Fab begins in explicit water solvent 1-2 nm above a lipid bilayer, freely diffusing and tumbling in bulk solvent, often resulting in a temporary or permanent insertion event (right).

(B,C,D) 18 replicates of coarse grain Fab systems (4E10, PGZL1, 10E8, respectively), initialized with slightly different Fab orientations relative to lipid bilayer. Frames with Fab contacting the membrane are in green and frames with Fab in water (non-associated) are in white for replicate trajectories of 14 µs each.

(E) 18 replicates of coarse grain BSA (top) or 13h11 (bottom) with different starting orientations relative to the lipid bilayer. Membrane contact (green) or diffusion in water (white) shown over 10 µs time.

(F) Snapshots describing a co-assembling membrane pipeline with 4E10 Fab. An Fab is centered in a box with various rotational orientations in space, explicit water, and lipids randomly arranged within a subset of the box (left). By 30ns, the membrane is fully formed (middle). Fab molecules result in a pre-docked membrane bound conformation and sample a permanent insertion event, intermittent membrane association, or dissociation depending on how the Fab contacts with the membrane (right).

(G, H, I) 40 replicates of 5 µs simulations for coarse grain co-assembling systems (4E10, PGZL1, 10E8, respectively), each with slightly different Fab initial orientations relative to lipid bilayer. Membrane contact is classified as above.

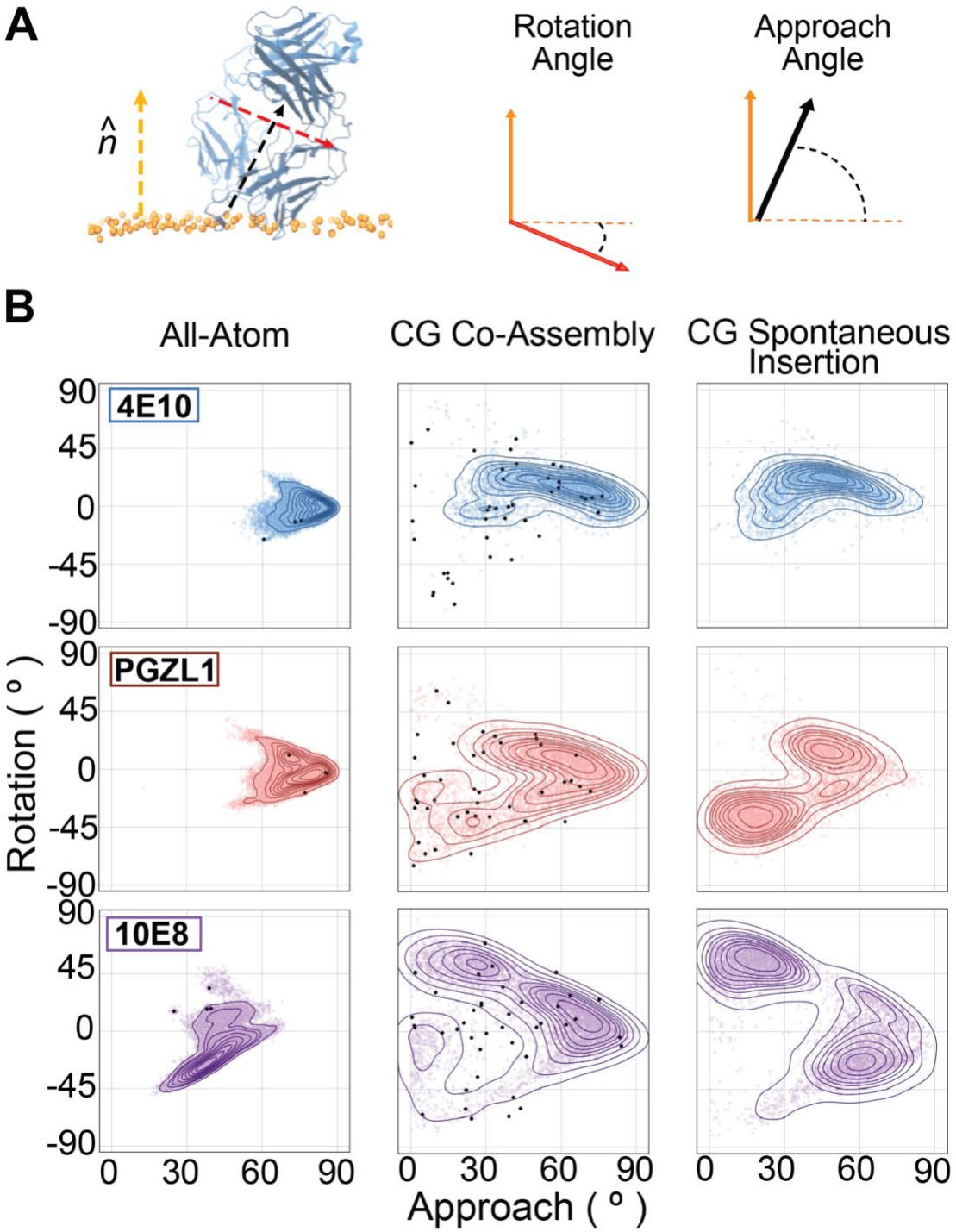

Figure 5. Membrane surface-bound bnAb conformations sampled across multiscale simulations
(A) Graphic of angles defined to describe Fab geometries relative to the normal vector at the membrane's upper leaflet lipid at the phosphate plane in simulation frames (orange arrow). The canonical "approach angle" defines the long axis of the Fab domain (i.e. the central pseudo-symmetry axis) and membrane normal vector (black arrow). A second "rotational angle" is defines the global domain rotation about the Fab pseudo-symmetry axis relative to the membrane normal vector, based on the short axis traversing the light and heavy chains, which is nearly orthogonal to the Fab's central axis (red arrow).
(B) Frequency plots of rotation and approach angles from frames of membrane-bound Fabs in MD simulations for 4E10 (blue, top row), PGZL1 (red, middle row), and 10E8 (purple, bottom row). Contour plots depicting frequency maxima for angle pairs sampled are by kernel density estimation. Left column, membrane interaction angles sampled from all-atom simulations with Fabs pre-docked using OPM PPM server prediction. Middle column, geometries from coarse-grain membrane co-assembly simulations. Right column, geometries from

unbiased spontaneous insertion coarse-grain simulations. Black dots denote the initial Fab-membrane geometries of starting states for replicate trajectories for each antibody initiated in the lipid bilayer.

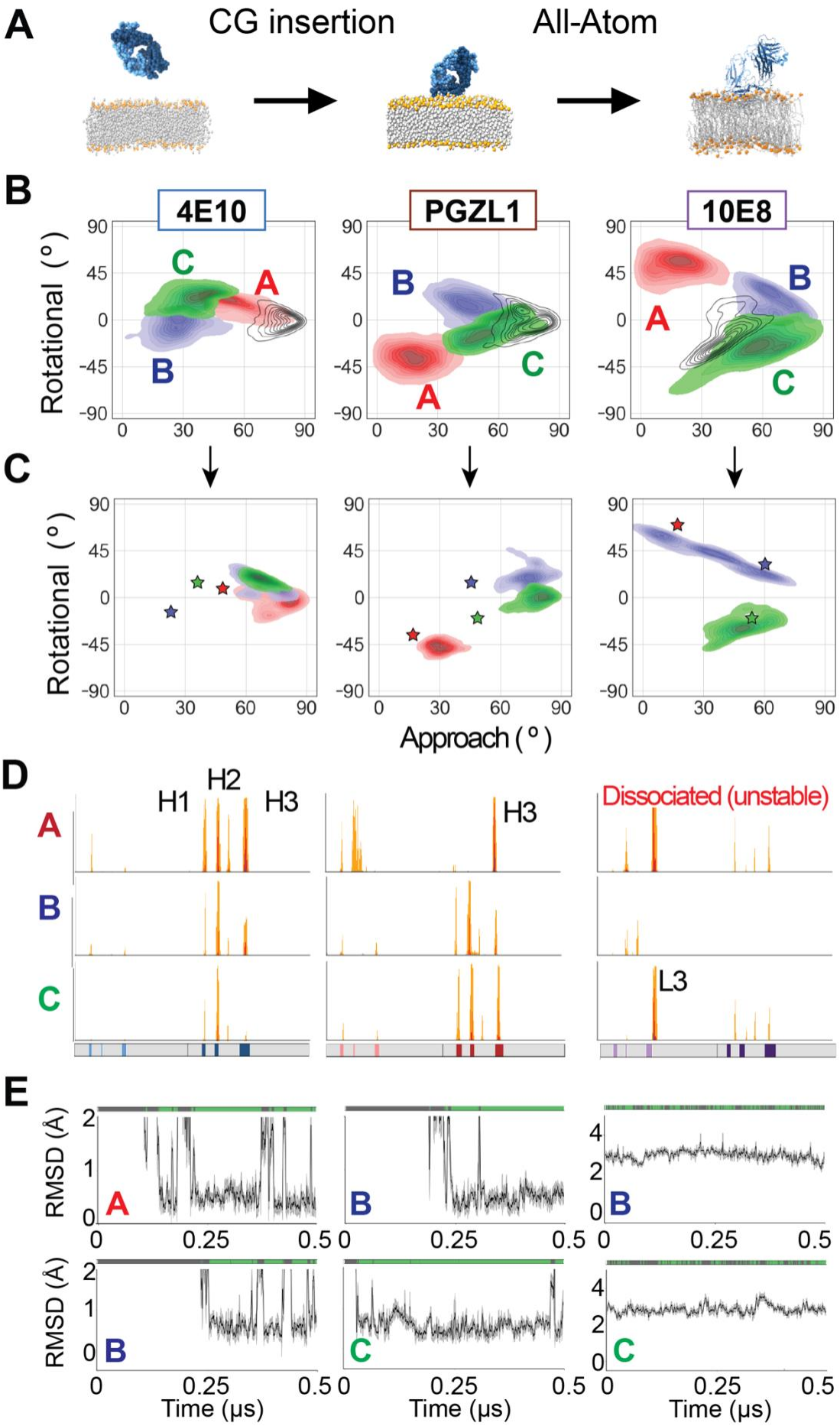
A
CG insertion
All-Atom
B
4E10
PGZL1
10E8
Rotational (°)
C
Approach (°)
D
H1
H2
H3
Dissociated (unstable)
L3
E
RMSD (Å)
Time (μs)

Figure 6. Back-mapping CG membrane-bound geometries to all-atom simulations allows integrative *ab initio* modeling of the full bnAb insertion process.

(A) Representative frames from membrane-bound 4E10 Fab coarse-grained simulations were back-mapped to all-atom representation to assess the stability and plausibility of those membrane-bound conformations. This coarse-grained-to-all-atom (CG-to-AA) reversion was applied for all medoid frames of interest from each antibody system and used to initiate half-microsecond unbiased all-atom dynamics simulations.

(B) Frequency of membrane interaction angles from coarse grain spontaneous insertion as clustered by geometric substates for 4E10, PGZL1 and 10E8, colored and contoured as in Fig 3B. Corresponding primary all-atom simulations is overlaid (unfilled, black contour frequency density plot).

(C) Conformational geometry sampled upon conversion of CG medoid to an all-atom trajectory. Initial geometry denoted by stars colored matching CG clusters in (**B**). Frequency and contour plots of conformational angles sampled in stably inserted backmapped all-atom trajectories for 4E10 (left), PGZL1 (middle), and 10E8 (right).

(D) Per-residue interaction profiles for antibody Fab simulations for 4E10 (left), PGZL1 (middle), 10E8 (right) representing each backmapped atomic trajectory, showing CDR-mediated conformations of differing depths and geometries.

(E) Phospholipid headgroup binding and RMSD plots of closest lipid at respective experimentally determined CDR sites for 4E10 (left), PGZL1 (middle), and 10E8 (right), plotted as in Figure 1C or 2B.

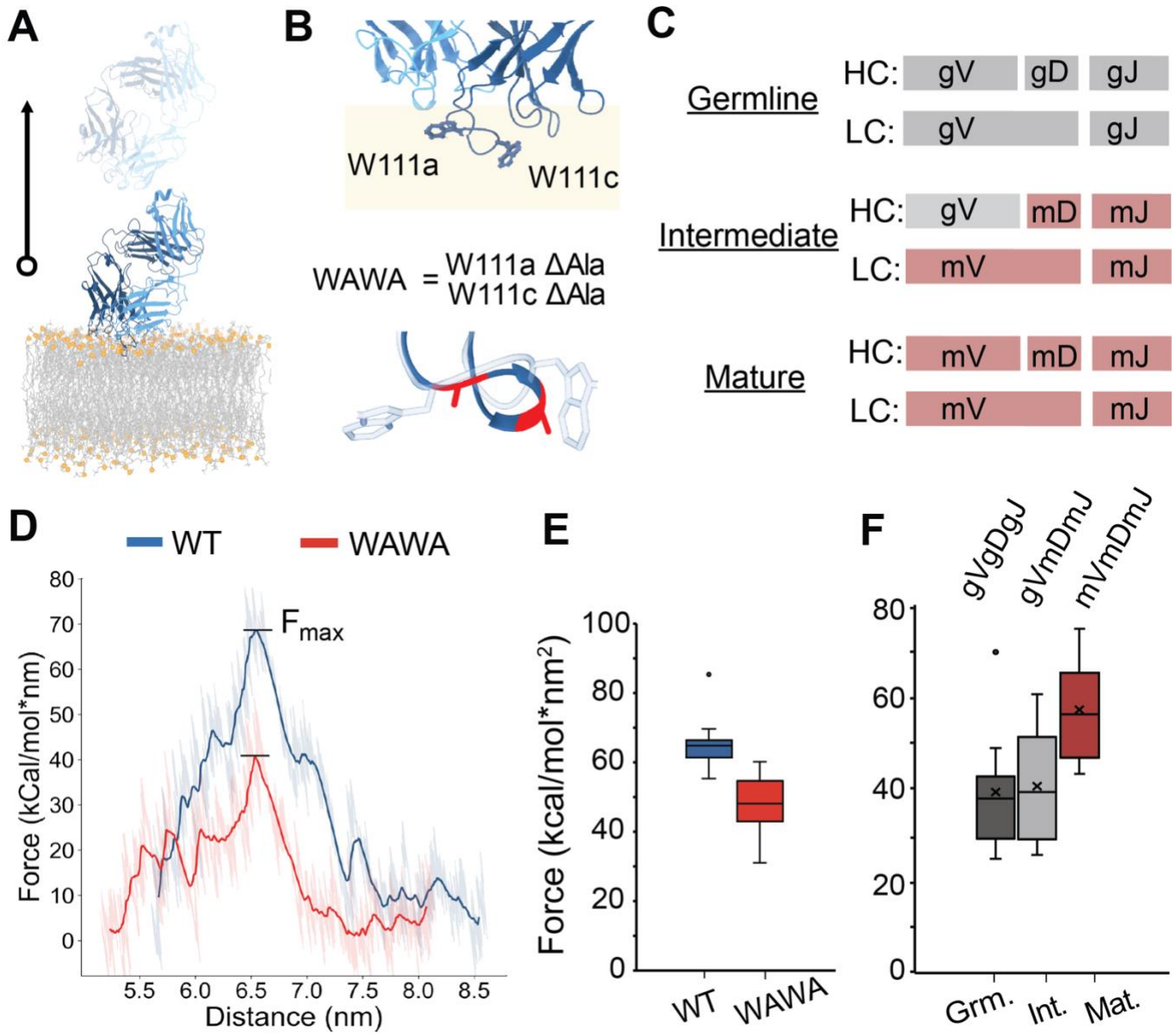

Figure 7. Biased antibody-membrane pulling dissociation simulations approximate Fab-membrane interaction strength for bnAb Fab variants of known lipid binding affinity or neutralization potency.

(A) Schematic of pulling method, a bnAbs Fabs associated with the lipid bilayers is subject to an applied upward dissociation force to the Fab domain center of mass at constant velocity to measure the force required to dissociate the Fab from the bilayer.

(B) The Trp100a-Trp100c motif residues in 4E10 CDR-H3 loop of expected to be lipid-embedded in the bilayer (beige). The double alanine mutant "WAWA" 4E10 variant has experimentally determined significantly reduced affinity to lipid bilayers and lower neutralization potency, due to lack of Trp membrane insertion.

(C) Previously experimentally characterized[20] PGZL1 germline-reverted variants, shown as chimera of germline versus matured gene segments, used to approximate antibody properties along its maturation trajectory.

(D) Average force versus distance plots and rupture force (F_{max}) calculation for one replicate of pulling wild type 4E10 (WT, blue) and 4E10 WAWA (red) to bias Fab dissociation from the bilayer.

(E) Distribution of rupture forces required for dissociation for different membrane-bound starting conformations for 4E10 (n=9, blue) and 4E10 WAWA (n=11, red), with starting conformations drawn from previous unbiased all-atom simulation ensembles at rest. Outliers as dots

(F) Distributions of rupture forces (n=10) required for membrane dissociation of PGZL1 inferred variants along the maturation pathway, for germline (dark grey, Grm.), intermediate (light grey, Int.), and mature (maroon, Mat.) PGZL1. Outliers as dots

References

1. Goodnow, C.C., Sprent, J., de St Groth, B.F., and Vinuesa, C.G. (2005). Cellular and genetic mechanisms of self tolerance and autoimmunity. Nature *435*, 590–597. 10.1038/nature03724.

2. Liu, M., Yang, G., Wiehe, K., Nicely, N.I., Vandergrift, N.A., Rountree, W., Bonsignori, M., Alam, S.M., Gao, J., Haynes, B.F., et al. (2015). Polyreactivity and Autoreactivity among HIV-1 Antibodies. J Virol *89*, 784–798. 10.1128/JVI.02378-14.

3. Verkoczy, L., Diaz, M., Holl, T.M., Ouyang, Y.-B., Bouton-Verville, H., Alam, S.M., Liao, H.-X., Kelsoe, G., and Haynes, B.F. (2010). Autoreactivity in an HIV-1 broadly reactive neutralizing antibody variable region heavy chain induces immunologic tolerance. Proc. Natl. Acad. Sci. U.S.A. *107*, 181–186. 10.1073/pnas.0912914107.

4. Zhang, R., Verkoczy, L., Wiehe, K., Munir Alam, S., Nicely, N.I., Santra, S., Bradley, T., Pemble, C.W., Zhang, J., Gao, F., et al. (2016). Initiation of immune tolerance–controlled HIV gp41 neutralizing B cell lineages. Sci. Transl. Med. *8*. 10.1126/scitranslmed.aaf0618.

5. Matyas, G.R., Beck, Z., Karasavvas, N., and Alving, C.R. (2009). Lipid binding properties of 4E10, 2F5, and WR304 monoclonal antibodies that neutralize HIV-1. Biochimica et Biophysica Acta (BBA) - Biomembranes *1788*, 660–665. 10.1016/j.bbamem.2008.11.015.

6. Alam, S.M., McAdams, M., Boren, D., Rak, M., Scearce, R.M., Gao, F., Camacho, Z.T., Gewirth, D., Kelsoe, G., Chen, P., et al. (2007). The Role of Antibody Polyspecificity and Lipid Reactivity in Binding of Broadly Neutralizing Anti-HIV-1 Envelope Human Monoclonal Antibodies 2F5 and 4E10 to Glycoprotein 41 Membrane Proximal Envelope Epitopes. The Journal of Immunology *178*, 4424–4435. 10.4049/jimmunol.178.7.4424.

7. Alam, S.M., Morelli, M., Dennison, S.M., Liao, H.-X., Zhang, R., Xia, S.-M., Rits-Volloch, S., Sun, L., Harrison, S.C., Haynes, B.F., et al. (2009). Role of HIV membrane in neutralization by two broadly neutralizing antibodies. Proc. Natl. Acad. Sci. U.S.A. *106*, 20234–20239. 10.1073/pnas.0908713106.

8. Haynes, B.F., Fleming, J., St. Clair, E.W., Katinger, H., Stiegler, G., Kunert, R., Robinson, J., Scearce, R.M., Plonk, K., Staats, H.F., et al. (2005). Cardiolipin Polyspecific Autoreactivity in Two Broadly Neutralizing HIV-1 Antibodies. Science *308*, 1906–1908. 10.1126/science.1111781.

9. Caillat, C., Guilligay, D., Sulbaran, G., and Weissenhorn, W. (2020). Neutralizing Antibodies Targeting HIV-1 gp41. Viruses *12*, 1210. 10.3390/v12111210.

10. Burton, D.R., and Hangartner, L. (2016). Broadly Neutralizing Antibodies to HIV and Their Role in Vaccine Design. Annu. Rev. Immunol. *34*, 635–659. 10.1146/annurev-immunol-041015-055515.

11. Mascola, J.R., and Haynes, B.F. (2013). HIV-1 neutralizing antibodies: understanding nature's pathways. Immunol Rev *254*, 225–244. 10.1111/imr.12075.

12. Krebs, S.J., Kwon, Y.D., Schramm, C.A., Law, W.H., Donofrio, G., Zhou, K.H., Gift, S., Dussupt, V., Georgiev, I.S., Schätzle, S., et al. (2019). Longitudinal Analysis Reveals Early Development of Three MPER-Directed Neutralizing Antibody Lineages from an HIV-1-Infected Individual. Immunity *50*, 677-691.e13. 10.1016/j.immuni.2019.02.008.

13. Lee, J.H., Ozorowski, G., and Ward, A.B. (2016). Cryo-EM structure of a native, fully glycosylated, cleaved HIV-1 envelope trimer. Science *351*, 1043–1048. 10.1126/science.aad2450.

14. Cardoso, R.M.F., Brunel, F.M., Ferguson, S., Zwick, M., Burton, D.R., Dawson, P.E., and Wilson, I.A. (2007). Structural Basis of Enhanced Binding of Extended and Helically Constrained Peptide Epitopes of the Broadly Neutralizing HIV-1 Antibody 4E10. Journal of Molecular Biology *365*, 1533–1544. 10.1016/j.jmb.2006.10.088.

15. Cardoso, R.M.F., Zwick, M.B., Stanfield, R.L., Kunert, R., Binley, J.M., Katinger, H., Burton, D.R., and Wilson, I.A. (2005). Broadly Neutralizing Anti-HIV Antibody 4E10 Recognizes a Helical Conformation of a Highly Conserved Fusion-Associated Motif in gp41. Immunity *22*, 163–173. 10.1016/j.immuni.2004.12.011.

16. Sun, Z.-Y.J., Oh, K.J., Kim, M., Yu, J., Brusic, V., Song, L., Qiao, Z., Wang, J., Wagner, G., and Reinherz, E.L. (2008). HIV-1 Broadly Neutralizing Antibody Extracts Its Epitope from a Kinked gp41 Ectodomain Region on the Viral Membrane. Immunity *28*, 52–63. 10.1016/j.immuni.2007.11.018.

17. Stiegler, G., Kunert, R., Purtscher, M., Wolbank, S., Voglauer, R., Steindl, F., and Katinger, H. (2001). A Potent Cross-Clade Neutralizing Human Monoclonal Antibody against a Novel Epitope on gp41 of Human Immunodeficiency Virus Type 1. AIDS Research and Human Retroviruses *17*, 1757–1765. 10.1089/08892220152741450.

18. Huang, J., Ofek, G., Laub, L., Louder, M.K., Doria-Rose, N.A., Longo, N.S., Imamichi, H., Bailer, R.T., Chakrabarti, B., Sharma, S.K., et al. (2012). Broad and potent neutralization of HIV-1 by a gp41-specific human antibody. Nature *491*, 406–412. 10.1038/nature11544.

19. Pinto, D., Fenwick, C., Caillat, C., Silacci, C., Guseva, S., Dehez, F., Chipot, C., Barbieri, S., Minola, A., Jarrossay, D., et al. (2019). Structural Basis for Broad HIV-1 Neutralization by the MPER-Specific Human Broadly Neutralizing Antibody LN01. Cell Host & Microbe *26*, 623-637.e8. 10.1016/j.chom.2019.09.016.

20. Zhang, L., Irimia, A., He, L., Landais, E., Rantalainen, K., Leaman, D.P., Vollbrecht, T., Stano, A., Sands, D.I., Kim, A.S., et al. (2019). An MPER antibody neutralizes HIV-1 using germline features shared among donors. Nat Commun *10*, 5389. 10.1038/s41467-019-12973-1.

21. Scherer, E.M., Leaman, D.P., Zwick, M.B., McMichael, A.J., and Burton, D.R. (2010). Aromatic residues at the edge of the antibody combining site facilitate viral glycoprotein recognition through membrane interactions. Proc. Natl. Acad. Sci. U.S.A. *107*, 1529–1534. 10.1073/pnas.0909680107.

22. Chen, J., Frey, G., Peng, H., Rits-Volloch, S., Garrity, J., Seaman, M.S., and Chen, B. (2014). Mechanism of HIV-1 Neutralization by Antibodies Targeting a Membrane-Proximal Region of gp41. J Virol *88*, 1249–1258. 10.1128/JVI.02664-13.

23. Yang, G., Holl, T.M., Liu, Y., Li, Y., Lu, X., Nicely, N.I., Kepler, T.B., Alam, S.M., Liao, H.-X., Cain, D.W., et al. (2013). Identification of autoantigens recognized by the 2F5 and 4E10 broadly neutralizing HIV-1 antibodies. Journal of Experimental Medicine *210*, 241–256. 10.1084/jem.20121977.

24. Irimia, A., Serra, A.M., Sarkar, A., Jacak, R., Kalyuzhniy, O., Sok, D., Saye-Francisco, K.L., Schiffner, T., Tingle, R., Kubitz, M., et al. (2017). Lipid interactions and angle of approach to the HIV-1 viral membrane of broadly neutralizing antibody 10E8: Insights for vaccine and therapeutic design. PLoS Pathog *13*, e1006212. 10.1371/journal.ppat.1006212.

25. Kwon, Y.D., Chuang, G.-Y., Zhang, B., Bailer, R.T., Doria-Rose, N.A., Gindin, T.S., Lin, B., Louder, M.K., McKee, K., O'Dell, S., et al. (2018). Surface-Matrix Screening Identifies Semi-specific Interactions that Improve Potency of a Near Pan-reactive HIV-1-Neutralizing Antibody. Cell Reports *22*, 1798–1809. 10.1016/j.celrep.2018.01.023.

26. Zwick, M.B., Komori, H.K., Stanfield, R.L., Church, S., Wang, M., Parren, P.W.H.I., Kunert, R., Katinger, H., Wilson, I.A., and Burton, D.R. (2004). The Long Third Complementarity-Determining Region of the Heavy Chain Is Important in the Activity of the Broadly Neutralizing Anti-Human Immunodeficiency Virus Type 1 Antibody 2F5. J Virol *78*, 3155–3161. 10.1128/JVI.78.6.3155-3161.2004.

27. Rujas, E., Leaman, D.P., Insausti, S., Ortigosa-Pascual, L., Zhang, L., Zwick, M.B., and Nieva, J.L. (2018). Functional Optimization of Broadly Neutralizing HIV-1 Antibody 10E8 by Promotion of Membrane Interactions. J Virol *92*, e02249-17. 10.1128/JVI.02249-17.

28. Xu, H., Song, L., Kim, M., Holmes, M.A., Kraft, Z., Sellhorn, G., Reinherz, E.L., Stamatatos, L., and Strong, R.K. (2010). Interactions between Lipids and Human Anti-HIV Antibody 4E10 Can Be Reduced without Ablating Neutralizing Activity. J Virol *84*, 1076–1088. 10.1128/JVI.02113-09.

29. Julien, J.-P., Huarte, N., Maeso, R., Taneva, S.G., Cunningham, A., Nieva, J.L., and Pai, E.F. (2010). Ablation of the Complementarity-Determining Region H3 Apex of the Anti-HIV-1 Broadly Neutralizing Antibody 2F5 Abrogates Neutralizing Capacity without Affecting Core Epitope Binding. J Virol *84*, 4136–4147. 10.1128/JVI.02357-09.

30. Rantalainen, K., Berndsen, Z.T., Antanasijevic, A., Schiffner, T., Zhang, X., Lee, W.-H., Torres, J.L., Zhang, L., Irimia, A., Copps, J., et al. (2020). HIV-1 Envelope and MPER Antibody Structures in Lipid Assemblies. Cell Reports *31*, 107583. 10.1016/j.celrep.2020.107583.

31. Irimia, A., Sarkar, A., Stanfield, R.L., and Wilson, I.A. (2016). Crystallographic Identification of Lipid as an Integral Component of the Epitope of HIV Broadly Neutralizing Antibody 4E10. Immunity *44*, 21–31. 10.1016/j.immuni.2015.12.001.

32. Carravilla, P., Darré, L., Oar-Arteta, I.R., Vesga, A.G., Rujas, E., de las Heras-Martínez, G., Domene, C., Nieva, J.L., and Requejo-Isidro, J. (2020). The Bilayer Collective Properties Govern the Interaction of an HIV-1 Antibody with the Viral Membrane. Biophysical Journal *118*, 44–56. 10.1016/j.bpj.2019.11.005.

33. Soto, C., Ofek, G., Joyce, M.G., Zhang, B., McKee, K., Longo, N.S., Yang, Y., Huang, J., Parks, R., Eudailey, J., et al. (2016). Developmental Pathway of the MPER-Directed HIV-1-Neutralizing Antibody 10E8. PLoS One *11*, e0157409. 10.1371/journal.pone.0157409.

34. Lomize, M.A., Pogozheva, I.D., Joo, H., Mosberg, H.I., and Lomize, A.L. (2012). OPM database and PPM web server: resources for positioning of proteins in membranes. Nucleic Acids Research *40*, D370–D376. 10.1093/nar/gkr703.

35. Zwick, M.B., Labrijn, A.F., Wang, M., Spenlehauer, C., Saphire, E.O., Binley, J.M., Moore, J.P., Stiegler, G., Katinger, H., Burton, D.R., et al. (2001). Broadly Neutralizing Antibodies Targeted to the Membrane-Proximal External Region of Human Immunodeficiency Virus Type 1 Glycoprotein gp41. J Virol *75*, 10892–10905. 10.1128/JVI.75.22.10892-10905.2001.

36. Dennison, S.M., Stewart, S.M., Stempel, K.C., Liao, H.-X., Haynes, B.F., and Alam, S.M. (2009). Stable Docking of Neutralizing Human Immunodeficiency Virus Type 1 gp41 Membrane-Proximal External Region Monoclonal Antibodies 2F5 and 4E10 Is Dependent on the Membrane Immersion Depth of Their Epitope Regions. J Virol *83*, 10211–10223. 10.1128/JVI.00571-09.

37. Polizzi, N.F., and DeGrado, W.F. (2020). A defined structural unit enables de novo design of small-molecule–binding proteins. Science *369*, 1227–1233. 10.1126/science.abb8330.

38. Souza, P.C.T., Alessandri, R., Barnoud, J., Thallmair, S., Faustino, I., Grünewald, F., Patmanidis, I., Abdizadeh, H., Bruininks, B.M.H., Wassenaar, T.A., et al. (2021). Martini 3: a general purpose force field for coarse-grained molecular dynamics. Nat Methods *18*, 382–388. 10.1038/s41592-021-01098-3.

39. Ruggeri, F., Zhang, F., Lind, T., Bruce, E.D., Lau, B.L.T., and Cárdenas, M. (2013). Non-specific interactions between soluble proteins and lipids induce irreversible changes in the properties of lipid bilayers. Soft Matter *9*, 4219–4226. 10.1039/C3SM27769K.

40. Nicely, N.I., Dennison, S.M., Spicer, L., Scearce, R.M., Kelsoe, G., Ueda, Y., Chen, H., Liao, H.-X., Alam, S.M., and Haynes, B.F. (2010). Crystal structure of a non-neutralizing antibody to the HIV-1 gp41 membrane-proximal external region. Nat Struct Mol Biol *17*, 1492–1494. 10.1038/nsmb.1944.

41. Srinivasan, S., Zoni, V., and Vanni, S. (2021). Estimating the accuracy of the MARTINI model towards the investigation of peripheral protein–membrane interactions. Faraday Discuss. *232*, 131–148. 10.1039/D0FD00058B.

42. Corey, R.A., Vickery, O.N., Sansom, M.S.P., and Stansfeld, P.J. (2019). Insights into Membrane Protein–Lipid Interactions from Free Energy Calculations. J. Chem. Theory Comput. *15*, 5727–5736. 10.1021/acs.jctc.9b00548.

43. Montero, M., Gulzar, N., Klaric, K.-A., Donald, J.E., Lepik, C., Wu, S., Tsai, S., Julien, J.-P., Hessell, A.J., Wang, S., et al. (2012). Neutralizing Epitopes in the Membrane-Proximal External Region of HIV-1 gp41 Are Influenced by the Transmembrane Domain and the Plasma Membrane. J Virol *86*, 2930–2941. 10.1128/JVI.06349-11.

44. Williams, L.D., Ofek, G., Schätzle, S., McDaniel, J.R., Lu, X., Nicely, N.I., Wu, L., Lougheed, C.S., Bradley, T., Louder, M.K., et al. (2017). Potent and broad HIV-neutralizing antibodies in memory B cells and plasma. Sci. Immunol. *2*, eaal2200. 10.1126/sciimmunol.aal2200.

45. Jardine, J., Julien, J.-P., Menis, S., Ota, T., Kalyuzhniy, O., McGuire, A., Sok, D., Huang, P.-S., MacPherson, S., Jones, M., et al. (2013). Rational HIV Immunogen Design to Target Specific Germline B Cell Receptors. Science *340*, 711–716. 10.1126/science.1234150.

46. Steichen, J.M., Kulp, D.W., Tokatlian, T., Escolano, A., Dosenovic, P., Stanfield, R.L., McCoy, L.E., Ozorowski, G., Hu, X., Kalyuzhniy, O., et al. (2016). HIV Vaccine Design to Target Germline Precursors of Glycan-Dependent Broadly Neutralizing Antibodies. Immunity *45*, 483–496. 10.1016/j.immuni.2016.08.016.

47. Klein, F., Diskin, R., Scheid, J.F., Gaebler, C., Mouquet, H., Georgiev, I.S., Pancera, M., Zhou, T., Incesu, R.-B., Fu, B.Z., et al. (2013). Somatic Mutations of the Immunoglobulin Framework Are Generally Required for Broad and Potent HIV-1 Neutralization. Cell *153*, 126–138. 10.1016/j.cell.2013.03.018.

48. Briney, B., Inderbitzin, A., Joyce, C., and Burton, D.R. (2019). Commonality despite exceptional diversity in the baseline human antibody repertoire. Nature *566*, 393–397. 10.1038/s41586-019-0879-y.

49. Dema, B., and Charles, N. (2016). Autoantibodies in SLE: Specificities, Isotypes and Receptors. Antibodies *5*, 2. 10.3390/antib5010002.

50. Tao, T.-W., and Kriss, J.P. (1982). Membrane-Binding Antibodies in Patients with Graves' Disease and Other Autoimmune Diseases*. The Journal of Clinical Endocrinology & Metabolism *55*, 935–940. 10.1210/jcem-55-5-935.

51. Asherson, R.A. (2003). Antiphospholipid antibodies and infections. Annals of the Rheumatic Diseases *62*, 388–393. 10.1136/ard.62.5.388.

52. Sène, D., Piette, J.-C., and Cacoub, P. (2008). Antiphospholipid antibodies, antiphospholipid syndrome and infections. Autoimmunity Reviews *7*, 272–277. 10.1016/j.autrev.2007.10.001.